Determination of the beam asymmetry Σ in η- and η'-photoproduction using Bayesian statistics

JAKOB MICHAEL KRAUSE

Masterarbeit in Physik
angefertigt im Helmholtz-Institut für Strahlen- und Kernphysik

vorgelegt der
Mathematisch-Naturwissenschaftlichen Fakultät
der
Rheinischen Friedrich-Wilhelms-Universität
Bonn

Sep 2022

I hereby declare that this thesis was formulated by myself and that no sources or tools other than those cited were used.

Bonn, ...

Date Signature

1. Gutachterin: Jun. Prof. Dr. Annika Thiel
2. Gutachter: Prof. Dr. Jochen Dingfelder

Contents

1 Introduction **1**
- 1.1 Photoproduction of Pseudoscalar Mesons 4
- 1.2 Measurement of Polarization Observables 5
- 1.3 Introduction to Bayesian statistics 7
  - 1.3.1 Notation 7
  - 1.3.2 Bayes' theorem 8
  - 1.3.3 Markov-Chain-Monte-Carlo (MCMC) 8
  - 1.3.4 Comparison of Bayesian and Frequentist approach 9
  - 1.3.5 Combining inferences 9
- 1.4 Motivation and Structure of this Thesis 9

2 Experimental Setup **7**
- 2.1 Production of polarized high energy photon beam 8
  - 2.1.1 Goniometer 9
  - 2.1.2 Tagging system 9
- 2.2 Liquid hydrogen target 10
- 2.3 Detector system 11
  - 2.3.1 Inner detector 11
  - 2.3.2 Crystal Barrel and forward detector 12
  - 2.3.3 MiniTAPS 13
  - 2.3.4 Čerenkov detector 14
  - 2.3.5 Flux monitoring 14
- 2.4 Trigger 15
- 2.5 Software and Monte Carlo 15
  - 2.5.1 ExPLORA 16
  - 2.5.2 Monte Carlo 16
  - 2.5.3 Stan 17
- 2.6 Datasets 17

3 Event selection **19**
- 3.1 Reconstruction of events 20
- 3.2 Preselection and charge cut 20
- 3.3 Time of particles 21
- 3.4 Kinematic constraints 23
  - 3.4.1 Derivation of cut conditions 23
  - 3.4.2 Determination of cut ranges 24

3.4.3 Quality of event selection . . . 29
3.5 Investigation of background and additional cuts . . . 31
3.5.1 Inspecting plausibility of background reactions . . . 31
3.5.2 Misidentification of background reactions . . . 34
3.5.3 Examination of additional cuts . . . 39
3.6 Summary of event selection . . . 42
3.6.1 Reaction $\gamma p \to p\eta' \to p\gamma\gamma$ . . . 42
3.6.2 Reaction $\gamma p \to p\eta \to p\gamma\gamma$ . . . 43

4 Extraction of the beam asymmetries Σ_η and $\Sigma_{\eta'}$ 37
4.1 Methods . . . 38
4.1.1 Event yield asymmetries . . . 38
4.1.2 Event based fit . . . 41
4.2 Determination of Σ_η using Bayesian statistics . . . 44
4.2.1 Application of methods to toy Monte Carlo data . . . 44
4.2.2 Application of methods to data . . . 53
4.2.3 Discussion . . . 56
4.3 Determination of $\Sigma_{\eta'}$ . . . 58
4.3.1 Application of event based fit to toy Monte Carlo data . . . 58
4.3.2 Application of event based fit to data . . . 64
4.3.3 Systematic error . . . 68

5 Discussion of results 73
5.1 Comparison of results to existing data . . . 73
5.2 Comparison of results to PWA calculations . . . 75
5.3 Final discussion of methods . . . 77

5 Summary and outlook 73

A Illustration of used software tools 75
A.1 ExPLORA . . . 75
A.2 Stan . . . 76

B Additional plots and calculations 77
B.1 Statistical error for the asymmetry $A(\phi)$ . . . 77
B.2 Kinematic variables for each bin . . . 79
B.2.1 Coplanarity . . . 79
B.2.2 Polar angle difference . . . 81
B.2.3 Missing mass . . . 83
B.2.4 Invariant mass . . . 85

C Discussion of binned fits 87

D Investigation of posteriors without truncation 89

Bibliography 93

List of Figures 95

List of Tables 101

CHAPTER 1

Introduction

The *Standard Model of Particle Physics* (SM) is the most successful model aiming to describe the particles and forces of the universe. It distinguishes between *fermions* and *bosons*. While all matter consists of fermions, bosons are particles that mediate the fundamental interactions.

Matter consists of (anti-)quarks and (anti-)leptons with three generations of each. Table 1.1 shows all elementary fermions including some of their most important properties. Only the first and lightest generation consists of stable particles, i.e. the up and down quark as well as the electron and its neutrino. All other particles are heavier and not stable, they will thus decay fast via the strong, electromagnetic or weak interaction.

There are in fact four interactions described by the SM: strong, electromagnetic, weak and gravitational interaction [1], where gravitation is mentioned here for the sake of completeness; on the mass scale of elementary particles gravitation is negligible. Strong and weak interaction are restricted to a finite range of the order of the nucleon radius, whereas electromagnetic interaction and gravitation have infinite range. Each interaction has its own coupling (charge). The strong interaction is mediated by gluons and couples to the color charge.

	Generation			**el. charge**	**color charge**
	1	**2**	**3**		
Quarks	u	c	t	2/3	r,g,b
	d	s	b	1/3	r,g,b
Leptons	e	μ	τ	-1	-
	ν_e	ν_μ	ν_τ	0	-

Table 1.1: Summary of the particles of the SM

Gluons and quarks carry color charge and thus interact strongly. However, an isolated quark or gluon has not been observed. Only color neutral bound systems of quarks are seen, which are called hadrons. Hadrons with integer spin are called mesons and those with half-integer spin are called baryons. Color neutrality demands mesons consist of at least one quark and one anti-quark and baryons consist of at least three quarks.

[1] they are ordered here according to their relative strength

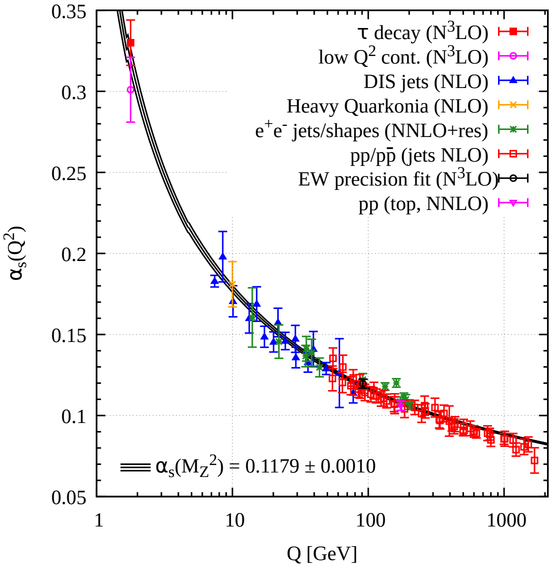

Figure 1.1: Running coupling of QCD. The colored data points represent different methods to obtain a value for α_s. For a detailed review see [Wor+22].

As already mentioned, isolated quarks are not seen. This can be understood in terms of the strong coupling constant α_s. The coupling constant is a measure of the strength of the strong interaction. Because it is highly dependent on the momentum transfer in the observed strong reaction it is also called running coupling constant, which is depicted in figure 1.1.

For low (< 1 GeV) momentum transfers or large distances the coupling constant approaches infinity whereas it decreases for high ($\gg 1$ GeV) momentum transfers or short distances. These momentum ranges are referred to as *confinement* and *asymptotic freedom*, respectively; quarks are confined to remain in a bound state since if one tried to pull them apart the color field becomes so strong it will create a new quark anti-quark pair resulting in two new bound states. On the other hand, bound quarks behave quasi-free and can be described using perturbative quantum chromodynamics (pQCD) if probed at sufficiently large momentum transfers.

It is more difficult however to describe QCD at momentum scales of ≈ 1 GeV since the coupling is too strong to justify a perturbative approach. Thus explicit modeling of QCD bound states is inevitable. One possibility is to describe baryons consisting of constituent quarks which are bound in a potential. Constituent quark models assume baryons are made up of three constituent quarks with effective masses differing from the bare quark mass. The effective mass is made up mostly from a sea of quark anti-quark pairs and gluons which surround the bare (valence) quarks. The explicit form of the binding potential is determined for each model.

The Bonn model [LMP01], for example, is formulated as a relativistically covariant constituent quark model. A potential increasing linearly with the distance is employed to adequately describe confinement. The binding potential between the constituent quarks is described by an instanton-induced interaction. Baryon resonances are then states with an orbital or angular excitation of one of the quarks. Figure 1.2 shows computed nucleon resonances with Isospin $I = 1/2$ of the Bonn model [LMP01] on the left side of each column. These are compared to measured resonances and their PDG rating [Wor+22] in the middle. Uncertainties are indicated by the colored areas. The resonances are identified by their total angular momentum and their parity $J\pi$. In addition also the total internal angular momentum along with isospin and again the total angular momentum $L_{2T\,2J}$ is given. While

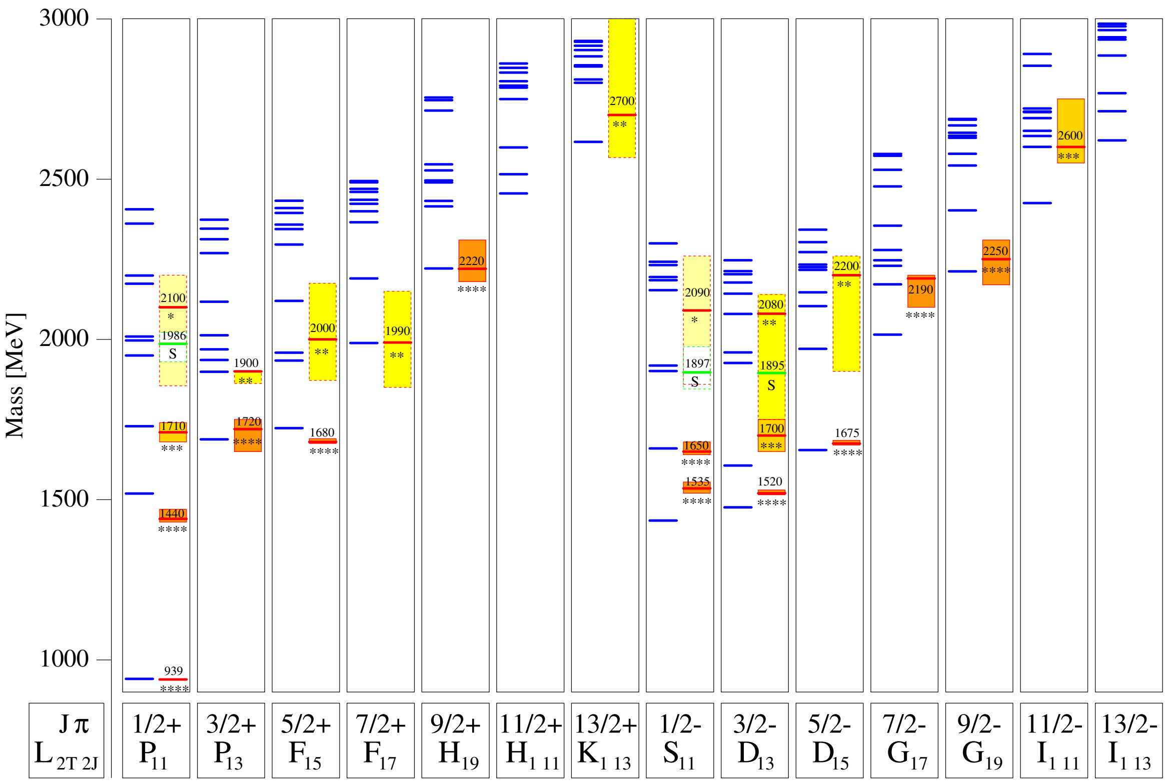

Figure 1.2: Calculated nucleon (isospin $I = 1/2$) resonances compared to measurements. Left in each column are the calculations [LMP01], the middle shows the measurements and PDG rating [Wor+22]

generally good agreement exists for low lying resonances, especially for high masses there are much more resonances predicted than actually found. This is also known as the problem of the "missing resonances" indicating the poor understanding of QCD in the non-perturbative region. This can be due to several reasons: most of the knowledge about nucleon resonances and their properties was obtained investigating the πN channel, biasing the data for resonances coupling weakly to this channel. Furthermore, the number of excited states with definite quantum numbers is related directly to the effective number of degrees-of-freedom accessible to the underlying theory. As a consequence, the number of degrees-of-freedom should be obtainable by comparing the measured states to the predicted states. Since nucleon resonances decay dominantly hadronic, their resonances are broad and overlapping. Thus on one hand the determination of excitation spectra proves to be a challenge on its own, demanding sophisticated methods, such as partial wave analysis (PWA). On the other hand it is not yet clear how many effective degrees-of-freedom exist for the nucleon in a constituent quark model. They could for example be decreased if the nucleon were made up of a quark and a di-quark structure. To access nucleon resonances and transitions between them for as many final states as possible the photoproduction of mesons off the proton has gained attention. Experiments dedicated to study photoproduction reactions off nucleons are located e.g. at JLAB, MAMI or ELSA. In this thesis photoproduction data taken at the CBELSA/TAPS experiment, which is located at the accelerator ELSA in Bonn, is analyzed regarding the reactions $\gamma p \to p\eta$ and $\gamma p \to p\eta'$. The theoretical foundation underlying the photoproduction of pseudoscalar mesons and the measurement of polarization observables will be discussed in the next sessions.

1.1 Photoproduction of Pseudoscalar Mesons

From the scattering theory point of view, photoproduction of mesons is well understood [KS03]. Figure 1.3 shows schematically the process thereof off the proton:

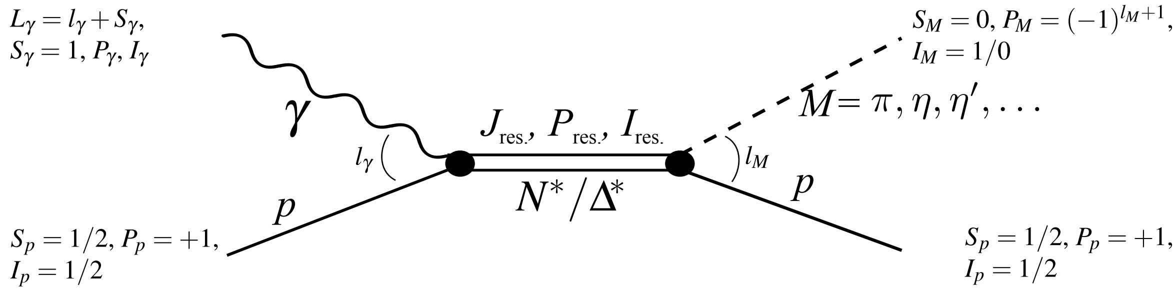

Figure 1.3: Feynman diagram for the s-channel photoproduction of pseudoscalar mesons, adapted from [Afz19]

The analysis requires partial wave decomposition in both initial and final states [DT92] since the intermediate resonance N^*/Δ^* has definite angular momentum, parity and isospin $J_{\text{res.}}, P_{\text{res.}}, I_{\text{res.}}$. The resonance is excited by a photon with (iso-) spin $I_\gamma, S_\gamma = 1$ and parity P_γ coupling electromagnetically to the target proton with (iso-) spin $I_p = 1/2, S_p = 1/2$ and parity P_p. The relative momentum is l_γ, such that the total momentum of the photon is $L_\gamma = l_\gamma + S_\gamma$. The parity of the photon depends on the multipolarity of the photon and is given by $P_\gamma = (-1)^{L_\gamma}$ for electric (E) or $P_\gamma = (-1)^{L_\gamma+1}$ for magnetic (M) photon multipoles [DT92]. Subsequently the intermediate state will have the quantum numbers $J_{\text{res.}}, P_{\text{res.}}, I_{\text{res.}}$ and decay into a proton with spin $S_p = 1/2$, parity $P_p = +1$ and isospin $I_p = 1/2$ under emission of a meson. Here, only pseudoscalar mesons that have vanishing spin $S_M = 0$, isospin I_M, relative orbital angular momentum l_M und Parity $P_M = (-1)^{l_M+1}$ are considered. Note that for η and η' mesons $I_M = 0$; this exclusively limits the intermediate resonances to N^* states since the strong interaction conserves isospin [Wor+22]. The following selection rules can be derived using parity and momentum conservation [KS03; Afz19]

$$J_{\text{res.}} = L_\gamma \oplus S_p = L_\gamma \oplus 1/2, \tag{1.1}$$

$$P_{\text{res.}} = P_p \cdot P_\gamma = P_\gamma, \tag{1.2}$$

$$J_{\text{res.}} = l_M \oplus S_p = l_M \oplus 1/2 \tag{1.3}$$

$$P_{\text{res.}} = P_p \cdot P_M = (-1)^{l_M+1}, \tag{1.4}$$

where the usual rules for the coupling $\oplus$ of angular momenta [Bar+18] apply. Thus, knowledge of the photoproduction multipoles allows the identification of contributing resonances for particular mesonic final states. Table 1.2 shows a summary of allowed quantum numbers according to the shown selection rules for the lowest order of photon multipoles ($L_\gamma = 1$). The photoproduction multipoles $E_{l\pm}, M_{l\pm}$ indicate the relative momentum of the meson ($l = l_M$) and whether the total angular momentum is obtained by adding "+" or substracting "–" the final state momenta. Resonances are identified in spectroscopic notation by the meson momentum l_M as well as by their (iso-)spin I, J and Mass M. Note that only $2I = 1$ resonances are listed since the mesons η and η' have vanishing isospin, so that only $I = 1/2$ resonances (N^* resonances) may be accessed. The determination

Photon multipole	**initial state** $\left(L_\gamma^{P_\gamma}, S_p^{P_p}\right)$	**intermed. state** $J_{\text{res}}^{P_{\text{res}}}$	**final state** $\left(S_p^{P_p}, l_M^{P_M}\right)$	**photoproduction multipole** $E_{l\pm}, M_{l\pm}$	**resonance** $\left(l_M\right)_{2I2J}\ (M)$
$E1$	$\left(1^-, \frac{1}{2}^+\right)$	$\frac{1}{2}^-$	$\left(\frac{1}{2}^+, 0^-\right)$	E_{0+}	$S_{13}(M)$
$E1$	$\left(1^-, \frac{1}{2}^+\right)$	$\frac{3}{2}^-$	$\left(\frac{1}{2}^+, 2^-\right)$	E_{2-}	$D_{13}(M)$
$M1$	$\left(1^+, \frac{1}{2}^+\right)$	$\frac{1}{2}^+$	$\left(\frac{1}{2}^+, 1^+\right)$	M_{1-}	$P_{11}(M)$
$M1$	$\left(1^+, \frac{1}{2}^+\right)$	$\frac{3}{2}^+$	$\left(\frac{1}{2}^+, 1^+\right)$	M_{1+}	$P_{13}(M)$

Table 1.2: Allowed quantum numbers for the intermediate resonance state N^* in η/η'-photoproduction. Adapted from [Afz19]

of contributing multipoles which can then be used to identify nucleon resonances is challenging and requires sophisticated (model dependent) partial wave analyses (PWA). The measurement of polarization observables helps to eliminate ambiguities in PWA calculations as will be explained in the following section.

1.2 Measurement of Polarization Observables

Using an ansatz purely motivated by scattering theory, the differential cross section of meson photoproduction can be written as

$$\frac{\mathrm{d}\sigma}{\mathrm{d}\Omega} = \frac{q}{k} \left|\langle f|\mathcal{F}|i\rangle\right|^2, \tag{1.5}$$

where the matrix element is taken between initial and final Pauli spinors [Che+57] and q and k denote the momentum of the incident photon and final state meson, respectively. The photoproduction amplitude $\mathcal{F}$ contains all relevant information regarding the scattering process connecting the initial and final state in analogy to the S-matrix that is introduced in the general discussion of quantum-mechanical scattering [PS95]. Following the notation of reference [Che+57] it can be written as a sum of the complex Chew-Goldberger-Low-Nambu (CGLN) amplitudes F_i

$$\mathcal{F} = i(\vec{\sigma} \cdot \vec{\epsilon})F_1 + (\vec{\sigma} \cdot \hat{q})(\vec{\sigma} \cdot (\hat{k} \times \vec{\epsilon}))F_2 + i(\vec{\sigma} \cdot \hat{k})(\hat{q} \cdot \vec{\epsilon})F_3 + i(\vec{\sigma} \cdot \hat{q})(\hat{q} \cdot \vec{\epsilon})F_4, \tag{1.6}$$

where $\hat{k}$ and $\vec{\epsilon}$ are the momentum unit vector and polarization vector of the incident photon, $\hat{q}$ is the momentum unit vector of the final state meson and $\vec{\sigma}$ denote the Pauli matrices. Applying the method of partial waves onto the complex CGLN amplitudes F_i one can absorb the angular dependence into Legendre polynomials $P_l(\cos\theta)$ and derivatives thereof [2] and express the energy dependence solely

[2] Here $\cos\theta$ denotes the polar angle of the meson in the center of mass system

by the photoproduction multipoles $E_{l\pm}, M_{l\pm}$, e.g. for F_1 one finds[Che+57]

$$F_1 = \sum_{l=0}^{\infty} \left[l M_{l+}(W) + E_{l+}(W) \right] P'_{l+1}(\cos\theta) + \left[(l+1) M_{l-}(W) + E_{l-}(W) \right] P'_{l-1}(\cos\theta), \tag{1.7}$$

where W is the center of mass energy. Inserting the partial wave expansion of all CGLN amplitudes into Equation (1.5) directly connects the CGLN amplitudes and the photoproduction multipoles to the cross section which is a measurable quantity. However, the measurement of the differential cross section will give one real number which is not sufficient to unambigously determine four complex amplitudes. To be able to access further observables that are connected to the CGLN amplitudes and the photoproduction multipoles, a polarized target and/or a polarized photon beam can be employed. In total, one may measure 16 non-redundant polarization observables [San+11] that are grouped into four categories: single polarization observables, where either the beam photon, target proton or recoil proton are polarized, and three groups of double polarization observables where two of the mentioned particles are polarized, i.e. the three groups are beam-target (BT), beam-recoil (BR) and target-recoil (TR) observables. In Table 1.3 all single and double polarization observables in pseudoscalar meson photoproduction are listed. Eight carefully chosen observables allow an unambigous determination of all CGLN amplitudes [CT97], which are then referred to as a *complete experiment* [CT97; San+11].

category	**observables**			
non /single	$\frac{\mathrm{d}\sigma}{\mathrm{d}\Omega}$ /	Σ	T	P
beam-target	G	H	E	F
beam-recoil	$O_{x'}$	$O_{z'}$	$C_{x'}$	$C_{z'}$
target-recoil	$T_{x'}$	$T_{z'}$	$L_{x'}$	$L_{z'}$

Table 1.3: All 16 non redundant polarization observables in pseudoscalar meson photoproduction [San+11]. Table adapted from [Afz12].

The CBELSA/TAPS experiment is able to produce a linearly or circularly polarized photon beam as well as a longitudinally or transersely polarized target. This introduces dependencies on the azimuthal angle into the differential cross section that couple to polarization observables Σ, T, P, E, F, G, H and the linear or circular polarization degrees of the photon beam $p_\gamma^{\text{lin}}, p_\gamma^{\text{circ}}$ as well as the target polarization p_x, p_y, p_z[San+11]

$$\begin{aligned} \frac{d\sigma}{d\Omega}\left(E_\gamma, \theta, \varphi\right) = \frac{d\sigma}{d\Omega}\left(E_\gamma, \theta\right) \Big[1 - p_\gamma^{\text{lin}} \mathbf{\Sigma} \cos(2\varphi) + p_x \left(p_\gamma^{\text{lin}} \mathbf{H} \sin(2\varphi) + p_\gamma^{\text{circ}} \mathbf{F} \right) \\ - p_\gamma \left(p_\gamma^{\text{lin}} \mathbf{P} \cos(2\varphi) - \mathbf{T} \right) - p_z \left(- p_\gamma^{\text{lin}} \mathbf{G} \sin(2\varphi) + p_\gamma^{\text{circ}} \mathbf{E} \right) \Big]. \end{aligned} \tag{1.8}$$

In this thesis data was analyzed that was taken with a linearly polarized photon beam and an unpolarized target, so that (1.8) reduces to

$$\frac{d\sigma}{d\Omega}\left(E_\gamma, \theta, \varphi\right) = \frac{d\sigma}{d\Omega}\left(E_\gamma, \theta\right) \left[1 - p_\gamma^{\text{lin}} \mathbf{\Sigma} \cos(2\varphi) \right], \tag{1.9}$$

which allows the determination of the beam asymmetry Σ, as is described in detail in chapter **??**. The beam asymmetry can then be related to the CGLN amplitudes in order to enable the determination of photoproduction multipoles if it is multiplied by the unpolarized cross section [FTS92]

$$\widehat{\Sigma} = \Sigma \cdot \left(\frac{\mathrm{d}\sigma}{\mathrm{d}\Omega}\right)_0 \propto \frac{\sin^2(\theta)}{2} \mathfrak{R} \left[\left|F_3\right|^2 + \left|F_4\right|^2 + 2\left(F_1^* F_4 + F_2^* F_3 + \cos\theta F_3^* F_4\right)\right]. \tag{1.10}$$

Unlike the unpolarized cross section, the beam asymmetry, or rather polarization observables in general, is sensitive not only to the absolute values of the photoproduction multipoles squared but is also sensitive to interference terms thereof [Afz19; Wun+17]. Ultimately the photoproduction multipoles can be linked to resonance properties like mass M and width Γ using (model dependent) partial wave analyses that consider many observables in different final states at once. Expanding the database of polarization observables helps to further eliminate ambiguities in the photoproduction multipoles, which are used to identify contributing resonances, and thus adds to the understanding of the strong interaction in the non perturbative regime.

1.3 Introduction to BAYESIAN statistics

To determine the beam asymmetry (see Chapter **??**) BAYESIAN methods are applied. This section will give a short introduction of the used concepts regarding BAYESIAN inference and the implementation of such a BAYESIAN analysis.

1.3.1 Notation

First of all, a probabilistic notation is introduced that will consequently be used throughout the remainder of this thesis to ease the formulation of BAYESIAN models and inferences. Hereby the BAYESIAN approach is directly applied to the context of parameter inference.

BAYESIAN parameter inference aims to draw statistical conslusions about parameters $\boldsymbol{\theta} = \{\theta_1, \theta_2, \ldots, \theta_N\}$ conditioned on observed data y in the form of probability statements [Gel+14]. The probability density of the introduced parameters $\boldsymbol{\theta}$ *given* the observed data y is written as

$$p(\boldsymbol{\theta}|y). \tag{1.11}$$

Distributions that are not conditioned on other observables, i.e. marginal or prior distributions, are notated as e.g.

$$p(\boldsymbol{\theta}). \tag{1.12}$$

If a parameter θ follows a well known probability density function (PDF) like a GAUSSIAN $\mathcal{N}$ with mean μ and standard deviation σ or POISSON distribution $\mathcal{P}$ with mean $\tilde{\mu}$ this is notated as

$$\theta \sim \mathcal{N}(\mu, \sigma) \qquad \Leftrightarrow \qquad p(\theta) = \mathcal{N}(\theta|\mu, \sigma) = \frac{1}{\sqrt{2\pi\sigma^2}} e^{-\frac{(\theta-\mu)^2}{2\sigma^2}}, \tag{1.13}$$

$$\tilde{\theta} \sim \mathcal{P}(\tilde{\mu}) \qquad \Leftrightarrow \qquad p(\tilde{\theta}) = \mathcal{P}(\tilde{\theta}|\tilde{\mu}) = \frac{\tilde{\mu}^{\theta}}{\tilde{\theta}!} e^{-\tilde{\mu}}. \tag{1.14}$$

1.3.2 Bayes' theorem

Bayes' theorem allows to link the conditional probabilities $p(\boldsymbol{\theta}|y)$ and $p(y|\boldsymbol{\theta})$ and can be formulated as [Gel+14]

$$p(\boldsymbol{\theta}|y) = \frac{p(y|\boldsymbol{\theta}) \cdot p(\boldsymbol{\theta})}{p(y)}. \tag{1.15}$$

In this context, $p(y|\boldsymbol{\theta})$ is called the *likelihood* that the data y are described by the parameters $\boldsymbol{\theta}$. The second factor in the enumerator on the right hand side of Eq. (1.15) is called the *prior* of the parameters $\boldsymbol{\theta}$. It gives their probability density prior to acquiring any information from the model. The denominator $p(y)$ is a normalizing constant, for which it holds

$$p(y) = \int_{\boldsymbol{\theta}} \mathrm{d}\boldsymbol{\theta} p(y|\boldsymbol{\theta}) \cdot p(\boldsymbol{\theta}). \tag{1.16}$$

With increasing complexity of the investigated data and model, evaluating the integral (1.16) can become challenging, if not impossible. But since for a fixed dataset it is in fact only a normalizing constant, one can choose to not evaluate it to arrive at the unnormalized *posterior* on the left hand side of Eq. 1.15 and 1.17

$$p(\boldsymbol{\theta}|y) \propto p(y|\boldsymbol{\theta}) \cdot p(\boldsymbol{\theta}). \tag{1.17}$$

The posterior gives the probability density function of the parameters $\boldsymbol{\theta}$ conditioned on the observed data y. For each parameter $\theta_n \in \boldsymbol{\theta}$ a one dimensional marginal posterior can be determined by integrating out all other parameters [SS05]

$$p(\theta_n|y) = \int \mathrm{d}\theta_1 \cdots \int \mathrm{d}\theta_{n-1} \int \mathrm{d}\theta_{n-1} \cdots \int \mathrm{d}\theta_N p(\theta_1 \dots \theta_N|y). \tag{1.18}$$

Determining marginal posteriors is the main goal of a Bayesian parameter inference. They give probability densities for each individual parameter based on the observed data and are the equivalent to point estimates with error bars that are e.g. determined from a χ^2 parameter fit but at the same time yield full distributions as a result. The determination of marginal posteriors with the ansatz formulated in Eq. 1.18 can become a highly non-trivial task using analytical methods with increasing number of parameters and complexity of the investigated model, so that the use of Monte-Carlo sampling is a suitable approach.

1.3.3 Markov-Chain-Monte-Carlo (MCMC)

Consider using Eq. (1.17) to determine unnormalized marginal posteriors for all parameters $\boldsymbol{\theta}$ without carrying out the integrations (1.18). This can be achieved by approximating the multidimensional joint unnormalized posterior $p(\boldsymbol{\theta}|y)$ using a large number of simulation draws $\boldsymbol{\theta}^{(s)}$ and projecting out each parameter θ_n while ignoring all other parameters $\theta_{k\neq n}$ [Tro08]. Thus, to perform a parameter inference, the main task is to accomplish the drawing of samples $\boldsymbol{\theta}^{(s)}$ that follow the joint posterior in order to access the marginal posteriors.

Markov chains are a finite sequence of random variables $\boldsymbol{\theta}^1, \boldsymbol{\theta}^2 \dots \boldsymbol{\theta}^S$ where for each step t the quantity $\boldsymbol{\theta}^t$ only depends on the previous $\boldsymbol{\theta}^{t-1}$ and is independent of all other previous chain elements [Gel+14]. Such a chain is created by starting at some initial value $\boldsymbol{\theta}^0$ and generate new draws from a transition distribution $T_t(\boldsymbol{\theta}^t \boldsymbol{\theta}^{t-1})$. The transition probabilities T_t can be constructed such that the

MARKOV chain reaches a stationary distribution which is the desired joint posterior (1.17) [Gel+14; Nor97].

1.3.4 Comparison of BAYESIAN and Frequentist approach

Frequentist Approach

The traditional approach to this fitting problem is a χ^2 fit. Assume there are N precise predictors $\{x_i\}$ and corresponding measurements $\{y_i\}$ with measurement errors $\{\sigma_i\}$. Additionally, the data y is expected to follow a functional $y = f(x, \boldsymbol{\theta})$ with parameter(s) $\boldsymbol{\theta}$ and predictors x. Then the test statistic

$$\chi^2 = \sum_{i=1}^{N} \left[\frac{y_i - f(x_i; \boldsymbol{\theta})}{\sigma_i^2} \right] \tag{1.19}$$

can be minimized with respect to the parameters $\boldsymbol{\theta}$ giving according estimates with error bars which are calculated using error propagation from the original data points $\{y_i\}$. The minimization can be solved analytically in the case of linear functions by solving the equation system

$$\frac{\mathrm{d}}{\mathrm{d}\boldsymbol{\theta}} \chi^2 = 0$$

and otherwise numerically. The minimization of χ^2 to get best-fit estimates for the desired parameters can be motivated if one considers the likelihood $\mathcal{L}$ that the data follow the function f. It is given by

$$\ln \mathcal{L} = -\frac{1}{2} \sum_{i=1}^{N} \left[\frac{y_i - f(x_i; \boldsymbol{\theta})}{\sigma_i} \right]^2 - \sum_{i=1}^{N} \ln \sigma_i \sqrt{2\pi}, \tag{1.20}$$

if one assumes GAUSSIAN errors at each data point. To maximize the (log-) likelihood with respect to all parameters is then equivalent to minimizing χ^2. As a byproduct, the χ^2 fit also gives a goodness of fit estimate which is given by $\chi^2/\mathrm{NDF} \approx 1$, where NDF are the number of degrees of freedom. Significantly smaller or larger values indicate too small error estimates or a bad fit, respectively. [Bar89]

Bayesian approach

As an alternative

1.3.5 Combining inferences

1.4 Motivation and Structure of this Thesis

bla

Bibliography

[Wor+22] R. L. Workman et al., *Review of Particle Physics*, PTEP **2022** (2022) 083C01 (cit. on pp. 2–4).

[LMP01] U. Löring, B. Metsch and H. Petry, *The light-baryon spectrum in a relativistic quark model with instanton-induced quark forces*, The European Physical Journal A **10** (2001) 395, ISSN: 1434-601X, URL: `http://dx.doi.org/10.1007/s100500170105` (cit. on pp. 2, 3).

[KS03] B. Krusche and S. Schadmand, *Study of nonstrange baryon resonances with meson photoproduction*, Prog. Part. Nucl. Phys. **51** (2003) 399, arXiv: `nucl-ex/0306023` (cit. on p. 4).

[Afz19] F. N. Afzal, *Measurement of the beam and helicity asymmetries in the reactions* $\gamma p \to p\pi^0$ *and* $\gamma p \to p\eta$, PhD thesis: Rheinische Friedrich-Wilhelms-Universität Bonn, 2019, URL: `https://hdl.handle.net/20.500.11811/8064` (cit. on pp. 4, 5, 7).

[DT92] D. Drechsel and L. Tiator, *Threshold pion photoproduction on nucleons*, J. Phys. G **18** (1992) 449 (cit. on p. 4).

[Bar+18] M. Bartelmann et al., *Theoretische Physik 3 | Quantenmechanik*, 2018, ISBN: 978-3-662-56071-6 (cit. on p. 4).

[Che+57] G. F. Chew, M. L. Goldberger, F. E. Low and Y. Nambu, *Relativistic Dispersion Relation Approach to Photomeson Production*, Phys. Rev. **106** (6 1957) 1345, URL: `https://link.aps.org/doi/10.1103/PhysRev.106.1345` (cit. on pp. 5, 6).

[PS95] M. E. Peskin and D. V. Schroeder, *An Introduction to quantum field theory*, Reading, USA: Addison-Wesley, 1995 (cit. on p. 5).

[San+11] A. M. Sandorfi, S. Hoblit, H. Kamano and T.-S. H. Lee, *Determining pseudoscalar meson photoproduction amplitudes from complete experiments*, Journal of Physics G: Nuclear and Particle Physics **38** (2011) 053001, ISSN: 1361-6471, URL: `http://dx.doi.org/10.1088/0954-3899/38/5/053001` (cit. on p. 6).

[CT97] W.-T. Chiang and F. Tabakin, *Completeness rules for spin observables in pseudoscalar meson photoproduction*, Physical Review C **55** (1997) 2054, ISSN: 1089-490X, URL: `http://dx.doi.org/10.1103/PhysRevC.55.2054` (cit. on p. 6).

[Afz12] F. N. Afzal, *Analysis of Crystal Barrel Data - Measurement of the double polarization observable E in the reaction* $\vec{\gamma}\vec{p} \to \eta' p$, Master thesis: Rheinische Friedrich-Wilhelms-Universität Bonn, 2012 (cit. on p. 6).

[FTS92] C. G. Fasano, F. Tabakin and B. Saghai,
Spin observables at threshold for meson photoproduction, Phys. Rev. C **46** (1992) 2430 (cit. on p. 7).

[Wun+17] Y. Wunderlich, F. Afzal, A. Thiel and R. Beck,
Determining the dominant partial wave contributions from angular distributions of single- and double-polarization observables in pseudoscalar meson photoproduction, The European Physical Journal A **53** (2017),
URL: `https://doi.org/10.1140%2Fepja%2Fi2017-12255-0` (cit. on p. 7).

[Gel+14] A. Gelman et al., *Bayesian Data Analysis*, vol. 3, Chapman & Hall/CRC, 2014 (cit. on pp. 7–9).

[SS05] D. Sivia and J. Skilling, *Data Analysis – A Bayesian Tutorial*, vol. 2, Oxford University Press, 2005 (cit. on p. 8).

[Tro08] R. Trotta, *Bayes in the sky: Bayesian inference and model selection in cosmology*, Contemporary Physics **49** (2008) 71,
URL: `https://doi.org/10.1080%2F00107510802066753` (cit. on p. 8).

[Nor97] J. R. Norris, *Markov Chains*,
Cambridge Series in Statistical and Probabilistic Mathematics,
Cambridge University Press, 1997.

[Bar89] R. J. Barlow,
Statistics, A Guide to the Use of Statistical Methods in the Physical Sciences,
Wiley, 1989 (cit. on p. 9).

List of Figures

1.1 Running coupling of QCD. The colored data points represent different methods to obtain a value for α_s. For a detailed review see [Wor+22]. 2
1.2 Calculated nucleon (isospin $I = 1/2$) resonances compared to measurements. Left in each column are the calculations [LMP01], the middle shows the measurements and PDG rating [Wor+22] 3
1.3 Feynman diagram for the s-channel photoproduction of pseudoscalar mesons, adapted from [Afz19] 4

2.1 Overview of the experimental hall of the CBELSA/TAPS experiment. The electron beam from ELSA enters at the top right. M. Grüner in [Afz19] 7
2.2 Illustration of the bremsstrahlung process: An electron e^- is deflected in the Coloumb field of a nucleus in the radiator material. A photon γ is emitted and so the momentum q is transferred. 8
2.3 Left: Incoherent (green) and crystal (blue) bremsstrahlung intensities as a function of the photon energy. Right: The enhancement spectrum is given as the ratio of crystal to incoherent intensity spectrum. The dashed line at the bottom shows the calculated polarization degree. Both spectra are generated using ANB calculations. Taken from [Afz19]. 9
2.4 The goniometer holds several radiators that can be inserted onto the beam axis (b). Also available is a Møller radiator [**cb**]. 10
2.5 Top-down view of the tagging system consisting of dipole magnet (red) and scintillating bars and fibers [**tagger**]. Electrons are deflected by the magnet after the bremsstrahlung process. 10
2.6 Schematic overview of the liquid hydrogen target. Two tubes connected to a heat exchanger and the Kapton cell allow filling it with liquid hydrogen. M. Grüner in [Afz19]. 11
2.7 The inner detector with three layers of scintillating fibers. The inner two layers are tilted with respect to the outer layer. D. Walther in [Afz19]. 12
2.8 Crystal barrel calorimeter and forward detector are built such that they enclose the target and the inner detector. The forward detector consists of the first three rings (green base) of crystals which are additionally covered by plastic scintillators for charged particle identification. The definition of polar angle θ and azimuthal angle ϕ in the LAB system are indicated as well.D. Walther in [**urban**] 12
2.9 The MiniTAPS detector is made up of 216 BaF_2 crystals (grey). In front of each crystal, plastic scintillators are mounted for charged particle information. Taken from [**cb**]. 14

2.10 The two detectors FluMo and GIM are used to monitor the photon flux at different reaction rates. D. Walther in [Afz19]. 15

3.1 Distribution of event classes in $\eta' \rightarrow \gamma\gamma$ production 21
3.2 Time information of all final state particles and the beam photon for 3PED η' production 22
3.3 Reaction time t_r for 3PED and 2.5PED η' production. The yellow region indicate the sidebands while the purple colored interval is the selected prompt peak. 23
3.4 Coplanarity of the $p\eta'$ final state with all other cuts applied for the energy bin $1500\,\text{MeV} \leq E_\gamma < 1600\,\text{MeV}$. The vertical dashed lines show the cut ranges obtained from a gaussian fit to the data (open circles). The solid black histograms represent fitted MC data of $\eta' \rightarrow \gamma\gamma$ 27
3.5 Polar angle difference of the $p\eta'$ final state with all other cuts applied for the energy bin $1500\,\text{MeV} \leq E_\gamma < 1600\,\text{MeV}$. The vertical dashed lines show the cut ranges obtained from a gaussian fit to the data (open circles). The solid black histograms represent fitted MC data of $\eta' \rightarrow \gamma\gamma$ 28
3.6 Missing mass of the $p\eta'$ final state with all other cuts applied for the energy bin $1500\,\text{MeV} \leq E_\gamma < 1600\,\text{MeV}$. The vertical dashed lines show the cut ranges obtained from a fit to data (open circles) employing a Novosibirsk function. The solid colored histograms represent fitted MC data from relevant photoproduction reactions: in black η', in green π^0, in red η, in blue ω, in yellow $2\pi^0$, magenta $\pi^0\eta$. The turquoise histogram is the sum of all MC histograms. 29
3.7 Invariant mass of the $p\eta'$ final state with all other cuts applied for all energy and angular bins. The open circles represent the measured data, the solid colored histograms fitted MC data from relevant photoproduction reactions: in black η', in green π^0, in red η, in blue ω, in yellow $2\pi^0$ and in magenta $\pi^0\eta$. The turquoise histogram is the sum of all MC histograms. 30
3.8 Invariant mass of the $p\eta'$ final state with all other cuts applied for the energy bin $1500\,\text{MeV} \leq E_\gamma < 1600\,\text{MeV}$. The vertical dashed lines show the cut ranges obtained from a gaussian fit to the η' MC data (solid black histogram). The open circles represent the measured data, the solid colored histograms fitted MC data from relevant photoproduction reactions: in black η', in green π^0, in red η, in blue ω, in yellow $2\pi^0$ and in magenta $\pi^0\eta$. The turquoise histogram is the sum of all MC histograms. . . . 30
3.9 Acceptance for the reaction $\gamma p \rightarrow p\eta'$ after all cuts that have been discussed so far for 2.5PED and 3PED events 31
3.10 Fraction of background events in the analyzed beam energy and angular bins. 32
3.11 Acceptance for possible background contributions 33
3.12 Generated energies of γ_3 and γ_4 in $2\pi^0$ and $\pi^0\eta$ photoproduction MC data. The threshold of 20 MeV is marked by a vertical red line. E_{γ_4} is shown on the top, E_{γ_3} is shown on the bottom of each figure. 35
3.13 E_γ^{gen} vs. E_γ^{rec} of γ_1 and γ_2 for $2\pi^0$ (top) and $\pi^0\eta$ (bottom) production. The slope $E_\gamma^{\text{gen}} = E_\gamma^{\text{rec}}$ is marked by a solid line. 37
3.14 Polar angle difference $\Delta\theta$ between γ_2 and γ_3 of the $\pi^0\eta$ final state. 38
3.15 Illustration of the misidentification process during reconstruction. Enumeration of photons is now arbitrary. 38

3.16 Generated CMS angle $\cos\theta_{\text{gen.}}$ vs. reconstructed CMS angle $\cos\theta_{\text{rec.}}$ for both background reactions. The slope $\cos\theta_{\text{gen.}} = \cos\theta_{\text{rec.}}$ is indicated by the solid line. . . 39
3.17 Detector hits of the recoil proton, as obtained from MC data for the production of η', $2\pi^0$ and $\pi^0\eta$. CB: Crystal Barrel, FW: forward dector, MT: MiniTAPS 41
3.18 Difference in measured and calculated beam energy. Data points are shown as open circles, MC data as solid histograms: in black η', in green π^0, in red η, in blue ω, in yellow $2\pi^0$ and in magenta $\pi^0\eta$. The turquoise histogram is the sum of all MC histograms. 42
3.19 Invariant mass spectrum passing different stages in the event selection process. In the end clear peaks for all possibly produced mesons are visible. The vertical lines indicate the mean cut ranges over all energy and angle bins. 43
3.20 Invariant mass spectrum passing different stages in the event selection process. In the end clear peaks for all possibly produced mesons are visible. Taken from [Afz19]. . . 44

4.1 Left: Definition of angles α, ϕ, φ. Right: Photon momentum $\vec{k}$ and polarization $\vec{\epsilon}$ define the beam polarization plane while the reaction plane is defined by the recoil proton p and produced meson M. 37
4.2 Posterior predictive checks $p\left(A_{\text{rep}}\middle|A\right)$ from a Bayesian fit to the event yield asymmetries for six toy Monte Carlo bins are shown as distributions. The data points in the upper plot are the asymmetry $A(\phi)$, which was additionally fitted using a χ^2 fit (solid line). The goodness of fit is shown using p-values, which give the fraction $T\left(A_{\text{rep}} > A\right)$ of replicated samples greater than the original measured value, with propagated statistical error bars on the bottom of each plot. The expected mean value of $T\left(A_{\text{rep}} > A\right) = 0.5$ is indicated by the dashed line. 46
4.3 p values of all toy Monte Carlo bins. They are centered around their mean at 0.5, which is indicated by the dashed line, and show no bias towards higher or lower values, thus confirming an adequate fit. 47
4.4 Left: Combined posterior distributions of all 10000 fits normalized by their respective standard deviation. Right: Unaltered combined posterior distributions of all 10000 fits. A Gaussian fit was performed to determine mean μ and standard deviation σ of the distributions with results given on top. 47
4.5 Left: relative error $\frac{\sigma_{\text{MCSE}}}{\text{median}[p(\Sigma|y)]}$ Right: $\widehat{R}$ associated with the fit parameter Σ. Both are shown for all 10000 fits. The critical values that should not be exceeded are marked by dashed lines. 48
4.6 Combined posteriors for the beam asymmetries Σ and Σ^{bkg} from all 1000 event based fits. Left: Residuals Ξ Right: Unnormalized posterior distributions. A Gaussian fit is performed on the distributions with results for mean μ and standard deviation σ on top. 50
4.7 Combined posterior probabilities using the *pooled likelihood* approach. Left: Signal beam asymmetry, Right: background beam asymmetry. Mean and standard deviation as obtained from a Gaussian fit are shown on top 51
4.8 Left: relative error $\frac{\sigma_{\text{MCSE}}}{\text{median}[p(\Sigma|y)]}$ Right: $\widehat{R}$ associated with the fit parameter Σ. Both are shown for all 1000 fits. The critical values that should not be exceeded are marked by dashed lines. 51

4.9 Posterior predictive check using the draws of the detector coefficients a and b. Points with error bars are the polarization weighted sum of event yields. The dashed line is the mean of the predictive values while the solid opaque lines are representative of one simulation draw $a^{(s)}, b^{(s)}$. 52

4.10 Posterior predictive checks $p\left(A_{\text{rep}}\middle|A\right)$ from a Bayesian fit to the event yield asymmetries for all angular bins of the energy bin $1250\,\text{MeV} \leq E_\gamma < 1310\,\text{MeV}$. The data points in the upper plot are the asymmetry $A(\phi)$, which was additionally fitted using a χ^2 fit (solid line). The goodness of fit is shown using p-values, which give the fraction $T\left(A_{\text{rep}} > A\right)$ of replicated samples greater than the original measured value, with propagated statistical error bars on the bottom of each plot. The expected mean value of $T\left(A_{\text{rep}} > A\right) = 0.5$ is indicated by the dashed line. 54

4.11 p values generated using all fits. They are centered around their mean at 0.5, which is indicated by the dashed line, and show no bias towards higher or lower values, thus confirming an adequate fit. 55

4.12 Left: relative error $\frac{\sigma_{\text{MCSE}}}{\text{median}[p(\Sigma|y)]}$ Right: $\widehat{R}$ associated with the fit parameter Σ. Both are shown for all $11 \cdot 12$ binned fits to the asymmetry $A(\phi)$. The critical values that should not be exceeded are marked by dashed lines. 55

4.13 Left: relative error $\frac{\sigma_{\text{MCSE}}}{\text{median}[p(\Sigma|y)]}$ Right: $\widehat{R}$ associated with the fit parameter Σ. Both are shown for all $11 \cdot 12$ unbinned fits. The critical values that should not be exceeded are marked by dashed lines. 56

4.14 Posterior predictive check using the draws of the detector coefficients a and b for the kinematic bin $1250\,\text{MeV} \leq E_\gamma < 1310\,\text{MeV}, 0 \leq \cos\theta < 0.17$. Points with error bars are the polarization weighted sum of event yields. The dashed line is the mean of the predictive values while the solid opaque lines are representative of one simulation draw $a^{(s)}, b^{(s)}$. 57

4.15 Final results for the beam asymmetry Σ in η photoproduction off the proton for all kinematic bins obtained with Bayesian methods. They are compared with the results of a least squares fit and an unbinned fit as given in reference [Afz19]. All results agree within statistical error bars or within the widths of marginal posterior distributions. 59

4.16 Normalized residuals (left) and unaltered distribution (right) of all 10000 fits for the beam asymmetry $\Sigma = (1-\delta) \cdot \Sigma_1 + \delta \cdot \Sigma_2$. Gaussian fits are performed with results given on top of each plot. 61

4.17 Normalized residuals (left) and unaltered distribution (right) of all 10000 fits for the background beam asymmetry Σ_t^{bkg}. Gaussian fits are performed with results given on top of each plot. 62

4.18 Fitted efficiency function (red line) applied to the polarization weighted sum of event yields (data points) for one toy Monte Carlo bin. 12 bins in ϕ are built for demonstration. 62

4.19 Combined (added) posteriors of all 1000 fits. Left: Signal beam asymmetry Σ_1 Right: Background beam asymmetry Σ_t^{bkg}. A Gaussian fit is performed with results given on top. 63

4.20 Combined (added) posteriors of all fits for the fit parameter Σ_2^{true}. A Gaussian fit is performed which reproduces exactly the values that were used for the simulations. . . 64

4.21 MCMC diagnostics for the event based BAYESIAN fit. Left: MCSE, Right: $\widehat{R}$-value. The critical values not to be exceeded are marked by the dashed lines. 65
4.22 Posterior predictive checks of one toy Monte Carlo bin using the draws from the marginal posteriors of the detector coefficients a, b (opaque blue lines). The mean values are marked by the dashed line and follow the distribution of the data points which are the polarization weighted sum of event yields, using 12 ϕ bins. 65
4.23 Final results for the beam asymmetry Σ in η' photoproduction. Two sets of results are shown: The dark blue distributions and orange data points with errorbars are obtained with an unbinned fit that does not consider any background contributions. The light blue distributions and data points are obtained with the modified BAYESIAN fit and by correcting the point estimates according to Equation (4.42), respectively. All errors are statistical errors only. 67
4.24 Results for the additionally fitted Σ_2^{true} (distributions) compared with the underlying data points [**mahlbergphd**] with statistical errors. The error bars on average cover 1σ of the distributions, indicating a successful fit. All errors are statistical errors only. 68
4.25 MCMC diagnostics for the event based BAYESIAN fit. Left: MCSE, Right: $\widehat{R}$-value. The critical values not to be exceeded are marked by the dashed lines. 69
4.26 Posterior predictive checks of the kinematic bin $1700\,\text{MeV} \leq E_\gamma < 1800\,\text{MeV}, 0.67 \leq \cos\theta < 1$ using the draws from the marginal posteriors of the detector coefficients a, b (opaque blue lines). The mean values are marked by the dashed line and follow the distribution of the data points which are the polarization weighted sum of event yields, using 12 ϕ bins. 69
4.27 Final results for the beam asymmetry $\Sigma_{\eta'}$ for all energy and angular bins. Only the corrected results from the unbinned maximum likelihood fit and distributions from the modified BAYESIAN fit are shown. The bottom of each plot indicates the systematic error as gray bars. It was determined as previously discussed. 71

5.1 Results for the beam asymmetry $\Sigma_{\eta'}$ (orange errorbars and distributions) compared with the results for the energy bins $E_\gamma = 1569\,\text{MeV}, E_\gamma = 1676\,\text{MeV}, E_\gamma = 1729\,\text{MeV}$ reported in reference [**collins**] (black errorbars). Systematical errors are shown as grey bars. 74
5.2 Results for the beam asymmetry $\Sigma_{\eta'}$ (orange errorbars and distributions) compared with PWA solutions: etaMAID [**etaMAID**](dashed black line),. . . The errorbars only depict statistical error, the systematic error is shown as grey bars. 76

A.1 Example `.xml` file that was used to call the plugin `CBTetaprimeanalysis.cpp` (line 20) with several self defined options. 75
A.2 Example `.stan` file that can be used to perform a simple linear fit. 76

B.1 Coplanarity $\Delta\phi$ for all energy and angular bins. Data points are displayed as open circles, scaled Monte Carlo data belonging to η' photoproduction is displayed as solid histogram. The determined cut ranges are indicated by the dashed red lines. 79
B.1 Coplanarity $\Delta\phi$ for all energy and angular bins. Data points are displayed as open circles, scaled Monte Carlo data belonging to η' photoproduction is displayed as solid histogram. The determined cut ranges are indicated by the dashed red lines. 80

B.2 Polar angle difference $\Delta\theta$ for all energy and angular bins. Data points are displayed as open circles, scaled Monte Carlo data belonging to η' photoproduction is displayed as solid histogram. The determined cut ranges are indicated by the dashed red lines. . . 81

B.2 Polar angle difference $\Delta\theta$ for all energy and angular bins. Data points are displayed as open circles, scaled Monte Carlo data belonging to η' photoproduction is displayed as solid histogram. The determined cut ranges are indicated by the dashed red lines. . . 82

B.3 Missing mass m_x for all energy and angular bins. Data points are displayed as open circles, scaled Monte Carlo data belonging to η' (black), $2\pi^0$ (yellow) and $\pi^0\eta$ (magenta) photoproduction is displayed as solid histogram while their sum is displayed as turquoise histogram. The determined cut ranges are indicated by the dashed red lines. 83

B.3 Missing mass m_X for all energy and angular bins. Data points are displayed as open circles, scaled Monte Carlo data belonging to η' (black), $2\pi^0$ (yellow) and $\pi^0\eta$ (magenta) photoproduction is displayed as solid histogram while their sum is displayed as turquoise histogram. The determined cut ranges are indicated by the dashed red lines. 84

B.4 Invariant mass m_{meson} for all energy and angular bins. Data points are displayed as open circles, scaled Monte Carlo data belonging to η' (black), $2\pi^0$ (yellow), $\pi^0\eta$ (magenta), π^0 (green) and ω (blue) photoproduction is displayed as solid histogram while their sum is displayed as turquoise histogram. The determined cut ranges are indicated by the dashed red lines. 85

B.4 Invariant mass m_{meson} for all energy and angular bins. Data points are displayed as open circles, scaled Monte Carlo data belonging to η' (black), $2\pi^0$ (yellow), $\pi^0\eta$ (magenta), π^0 (green) and ω (blue) photoproduction is displayed as solid histogram while their sum is displayed as turquoise histogram. The determined cut ranges are indicated by the dashed red lines. 86

C.1 Fit performance in dependence of the number of bins. Left axis shows the mean μ of the distribution of the normalized residuals ξ, right axis shows the mean χ^2 of all fits. Squares simulate fits with statistics similar to the $\gamma p \to p\eta' \to p\gamma\gamma$ final state, triangles statistics similar to the $\gamma p \to p\eta \to p\gamma\gamma$ and final state, pentagons statistics similar to the $\gamma p \to p\pi^0 \to p\gamma\gamma$. Dotted red line indicates the ideal value of $\chi^2 = 1$, while the dashed blue line indicates the ideal mean of the normalized residuals at $\mu = 0$. 88

D.1 Combined posteriors of all 1000 fits without truncation for the signal beam asymmetry Σ_1 and the background beam asymmetry Σ_t. Left: normalized residuals Ξ, Right: unaltered added posterior distributions. Gaussian fits have been performed with results given on top of each plot. 90

D.2 Posterior distributions of Σ_1 (left) and Σ_t (right) combined in an independent likelihood pool. Gaussian fits to the distribution confirm the reproduction of the input values within 1σ. Note that only very few datapoints were available for the fits, because the distributions overwhelmingly converge into a single bin at ± 0.5, hence the large errors on the fit parameters. 91

List of Tables

1.1 Summary of the particles of the SM 1
1.2 Allowed quantum numbers for the intermediate resonance state N^* in η/η'-photoproduction. Adapted from [Afz19] 5
1.3 All 16 non redundant polarization observables in pseudoscalar meson photoproduction [San+11]. Table adapted from [Afz12]. 6

2.1 Summary of the key parameters of the 2013 beam time at CBELSA/TAPS taken for the measurement of the beam asymmetry Σ. Taken from [Afz19]. 17

3.1 The five most probable decay modes of the η and η' meson. The most probable further decay with according branching ratio is shown in brackets.[Wor+22] 19
3.2 Examined MC reactions that were used in sum for the fit 25
3.3 Fit functions and cut ranges for each kinematic variable 26
3.4 Total cross sections σ in the energy range 1500 to 1800 MeV, branching ratios (BR) to $n\gamma$ final states, maximum acceptance $\tilde{A}$ for signal and possible background contributions as well as the expected signal to background ratio R. References [**2pi0_cs**] and [**pi0eta_cs**] give the cross sections only up to roughly 1500 MeV, the given values are thus upper bounds. For the same reason, from reference [**3pi0cs**] only a lower bound can be estimated. For all other reactions a rough mean over the energy bins of interest is built. If the references provide only differential cross sections a crude integration in each angular bin is performed. In case only very few $\left(\mathcal{O}\left(10^1\right)\right)$ decays pass event selection, the acceptance is built in one global bin only for the respective reactions. This is indicated by the horizontal line. 34
3.5 Relative loss in signal and background events if a cut on ΔE is applied. 40

4.1 Summary of the complete setting of all toy Monte Carlo experiments for the event based fit. Values and table layout adapted from [Afz19]. 49
4.2 Summary of the complete setting of all toy Monte Carlo experiments for the event based fit. Table layout adapted from [Afz19]. 60